NUMERICAL STUDY ON THE EFFECT OF VARYING SPANWISE TWIST ON LOW-REYNOLDS-NUMBER FLAPPING FLIGHT

S. Premachandran and M. Giacobello
Air Vehicles Division, Defence Science and Technology Organisation,
506 Lorimer Street, Fishermans Bend, 3207, Melbourne, Australia
sarah.premachandran@dsto.defence.gov.au

Keywords: *flapping wing, insect, wing twist, low-Reynolds-number*

Abstract

The aerodynamics of a flexible flapping wing are investigated for the case of hovering flight. 3D Computational Fluid Dynamics (CFD) is used to simulate a wing undergoing sinusoidal flapping and feathering kinematics. The feathering amplitude is prescribed to vary linearly from root to tip, to explore the effect of wing twist on the production of lift and on the aerodynamic power requirement. It was found that wing performance is dependent mainly on the value of the reference feathering-angle amplitude at 2/3 span, and not on the degree of spanwise twisting. Optimal conditions for lift and efficiency were identified for different twist parameters. The peak-efficiency condition required a high degree of feathering and was characterized by small, coherent, attached structures. The optimal lift condition was found to require intermediate feathering, and the flowfield comprised larger, less coherent structures.

1 Introduction

The aerodynamics of flapping-wing flight is a topic of interest both from a biological perspective and for application to the design of micro-air vehicles (MAVs). In the low-Reynolds-number (low-*Re*) regime, in which MAVs operate, flapping-wing insects are able to fly with a higher efficiency and maneuverability than conventional fixed-wing aircraft [1]. The parameters influencing the performance of insect flapping flight include the flight environment, wing kinematics, wing morphology and time-varying deformation. This paper provides insight into the effect of wing deformation on the lift generation and power efficiency. The mode of deformation considered in this study is spanwise twisting. Studies on real insects (see, for example, [2]) have found that their wings can undergo a large degree of spanwise twisting during the flapping cycle: the chord incidence has been observed to vary linearly between root and tip by up to approximately 70°. Experimental and numerical studies have shown that spanwise twisting can have a significant effect on force magnitudes, resultant force direction and required input power [3], [4]. These studies, among others, have used either experimental models with flexible wings or fluid-structure interaction simulations using wings of different rigidity. The present work aims to numerically investigate the optimal flexibility characteristics from a purely aerodynamic standpoint. The effect of wing twist on aerodynamic forces and power requirements is therefore studied in isolation: a linear wing twist profile is prescribed, and the twist parameters are varied systematically.

2 Methodology

2.1 Problem Description

2.1.1 Geometry

The wing geometry and flapping kinematics

simulated were adapted from the water-tunnel experiments of Nagai, Isogai and Fujimoto [5]. Their rigid-wing experiment also serves as a validation point for the numerical simulations. The case of a single forewing in hovering flight is considered. The wing itself is of a rectangular planform, 250 mm in span and 50 mm in chord, with 2mm thickness and squared edges. The Reynolds number (*Re*) is 5500, based on the maximum wing velocity at 75% span (following [5]).

Two geometric boundary setups were used in this study. The first attempted to model the experimental conditions of Nagai *et al.* [5]. The outer boundary is based on the dimensions of the water-tunnel used in [5]. The width and height are 750mm and 380 mm respectively, and the splitter plate is modeled as a wall boundary in the *xz*-plane, 30mm from the global origin in keeping with [6] (Figure 2a). In the stream-wise direction (i.e. *z*-direction in Figure 1) the domain extended 0.5m upstream and 1.5m downstream of the stroke plane, to avoid stream-wise boundary interference.

The second domain (used in all other runs) is aimed towards simulating a pair of wings in a free open flow. The wing is modeled in a large hemispherical domain of radius 5m, with a symmetry plane in the same location as the tunnel's splitter plate.

2.1.2 Kinematics

The basic wing motion is a superposition of two types of rotation. The first, which will be referred to as 'flapping', is a back-and-forth rotation of the whole wing about the global *z*-axis, as shown in Figure 1. The *z=0* plane is referred to as the stroke plane. This motion is characterized by the instantaneous angle ϕ between the wing span in the stroke plane and the y-axis. The wing root is offset from the pivot origin by 65mm, in keeping with [5].

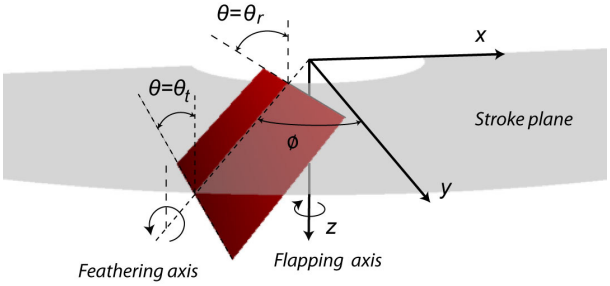

Figure 1 Coordinate system and kinematic parameter definition.

The second type of motion, 'feathering', is a back-and-forth rotation of the wing about a local axis which moves with the wing. This feathering axis is the line along the wing span at 30% chord from the leading edge (see Figure 1), and remains within the stroke plane. Feathering is quantified by the angle θ between the local chord and the global *z*-axis.

The instantaneous values of ϕ and θ are governed by

$$\begin{cases} \phi = \phi_0 \cos(2\pi t / T) \\ \theta = \theta_0 \cos(2\pi t / T + \xi) \end{cases}, \quad (1)$$

where T is the period of the flapping cycle. The phase lag ξ is fixed at $\pi/2$.

For the validation case, ϕ_0 =40° and θ_0 = 60°. Different values of θ_0 were also explored in the open-flow geometry. For the twist studies the value of the feathering amplitude θ_0 is varied linearly from the root value (θ_r) to the tip value (θ_t) as shown in Figure 1. Values of θ_r and θ_t ranging from 0° to 90° were considered to explore the aerodynamic effects. From a practical point of view, the θ_r=0° cases could correspond to a MAV application where the flapping angle is driven only from the root, and the feathering is allowed to occur passively. For the kinematics described it would generally be expected that $\theta_t > \theta_r$ (as observed for most insects [2]), as the flapping motion is driven close to the leading edge, and the centre of pressure is expected to be aft of this. However $\theta_t < \theta_r$ cases could be achieved though careful

configuration of the wing properties and pitch axis.

2.1.2 Performance Parameters

The performance parameters of interest are the lift (L) and power (P). Lift is the component of force normal to the stroke plane (the $-z$ direction in Figure 1). The aerodynamic power is calculated by summing up the dot product of the incremental force and velocity of the wing elements, i.e.:

$$P = \sum \partial F_i \bullet v_i \,. \tag{2}$$

The 'efficiency' (η) will be defined as the ratio of the cycle-averaged lift to total aerodynamic power consumed ($\eta = \overline{C}_L / \overline{C}_P$). The lift and power are non-dimensionalized using density ρ, and wing area A and a reference velocity (maximum velocity at 75% span, V_{ref}) according to

$$C_L = \frac{L}{\frac{1}{2}\rho V_{ref}^2 A} \quad , \qquad C_P = \frac{P}{\frac{1}{2}\rho V_{ref}^3 A} \tag{3}$$

2.2 Solver Methodology

2.2.1 Solution Parameters

The time-accurate, incompressible Navier–Stokes equations were solved directly using the finite-volume code Fluent v.12.1.2. [7]

For numerical stability, first-order accuracy was used for spatial discretization over the first four cycles, and the solution was then switched to second-order (i.e. second-order for pressure, second-order upwind for momentum, and the Green-Gauss Node-Based method for gradient). Temporal discretization was limited to first-order by the software when remeshing is used.

The simulations were run until the force histories stabilized to a periodic state. For the example of the validation case, over the 6th-10th cycles the instantaneous force values deviated by less than 2% from the averaged-cycle values, and the total lift over each cycle was found to deviate by less than 0.5% from the cycle-averaged mean total lift.

2.2.2 Remeshing

Due to the large wing motion amplitudes, and the necessity of maintaining a fixed symmetry plane (and tunnel boundaries, in the validation case), the software's built-in re-meshing capability was used to maintain a quality grid.

The two domains are illustrated in Figure 2 using a cut-through view of the stroke plane. The kinematics were imposed by moving the wing and a surrounding region of cells (the red area) according to the equations given in (1). The blue region is re-meshed periodically (approximately 60 times per cycle) to maintain good grid quality. For the non-tunnel runs, there is an additional outer (orange) region that is held fixed to avoid remeshing these cells (Figure 2b).

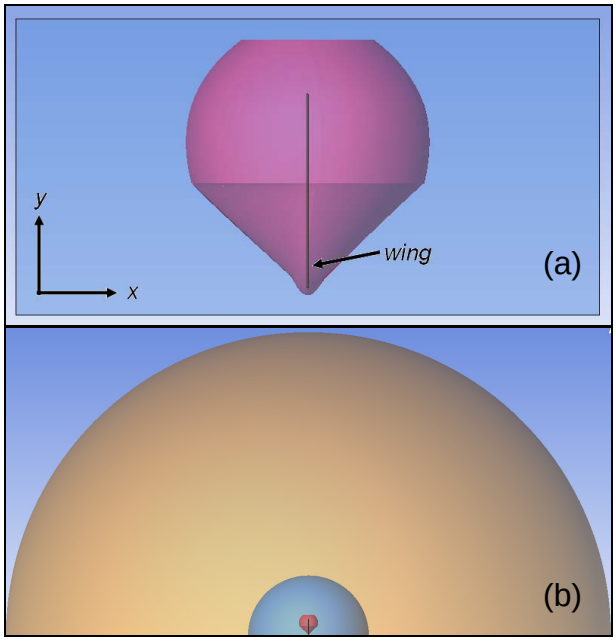

Figure 2 Cut-through ($z=0$ plane) of the computational domains; (a) validation case and (b) domain used in all other simulations.

2.2.3 Boundary Conditions

The wing surface was modeled as a no-slip wall condition. A symmetry plane was imposed along the *y*=0 plane (see Figure 1). For the validation case, this was to model the effect of the splitter plate used in [5]; for the other runs, the symmetry plane was intended to model a symmetric pair of wings. The outer boundary condition also varied with the simulation. For the validation case, the walls of the water tunnel used in [5] were replicated with no-slip wall conditions, and the inlet and outlet sides of the domain were modeled as pressure-inlet and pressure-outlet conditions. For the other cases, a pressure-outlet condition was used on the outer boundary.

2.3 Spatial Discretization

The domain was discretized using an unstructured mesh extending to the outer boundaries of the computational domain, with a structured boundary layer around the wing. The final mesh had a wing surface spacing ranging from 2mm (at the edges) to 4mm (i.e. 0.8%-1.6% of the span). The boundary layer had 5 layers, with the first node 2mm from the surface, growing exponentially to a total height of 11.5mm. For the non-tunnel runs, the cell size near the far-field boundary was increased in an effort to damp out the wake structures and avoid boundary interference effects which could contaminate the solution in the domain interior.

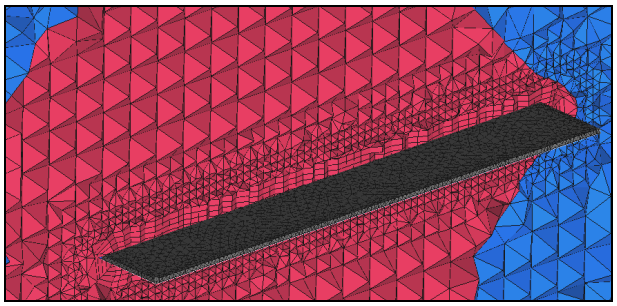

Figure 3 Close-up view of baseline mesh.

2.3 Verification and Validation

The sensitivity of the solution to changes in the size of the inner domain, the remeshing parameters, and the gradient solution method (Least-Squares Cell-Based vs Green-Gauss Node-based) were investigated. The boundary condition at the far-field (pressure-outlet versus inlet/outlet and pressure-far-field) was also explored.

To check grid independance, the wall-normal resolution was doubled, the first-layer height of the boundary layer was halved (with additional layers so that the total height remained approximately the same), and the volume meshing size parameters were halved throughout the domain. The resulting mesh comprised over double the number of elements (approximately 1.5 million, compared to the baseline mesh which comprised approximately 600,000). The lift over the averaged stroke-cycle differed by less than 4% of the range between the two meshes (as shown in Figure 4). Therefore the baseline mesh was considered to adequately resolve the flow and the corresponding mesh settings were used for the twisting studies.

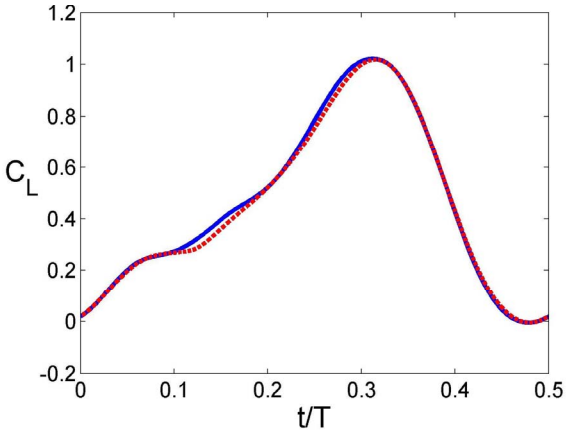

Figure 4 Grid independance study for validation case: baseline mesh (blue line) and finer mesh (red dashed line).

A time-step independence study was also performed. Timesteps-per-cycle (*ts/T*) values of 250, 500 and 1000 were considered. Figure 5 presents the computed lift over the averaged half-cycle along with corresponding results from [5]. The solution was found to change by

less than 3% by increasing *ts/T*. This difference is small, but since run times were not prohibitive, *ts/T* = 500 was used for all subsequent simulations. The peak lift is under-predicted by 8% compared to the experimental data, and overall, the agreement is considered acceptable.

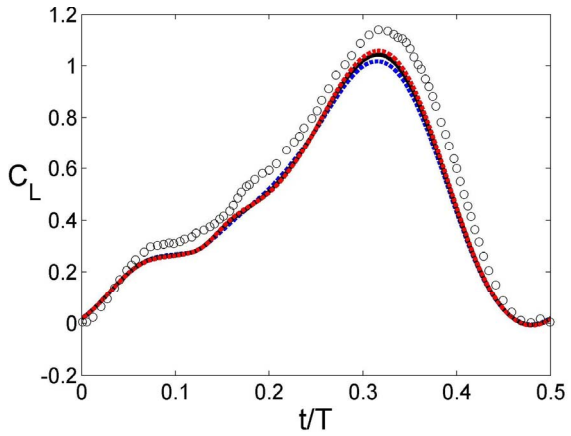

Figure 5 Time-step independance study for validation case: *ts/T*=250 (blue dashed line), *ts/T*=500 (black line) and *ts/T*=1000 (red dashed line). Experimental data reproduced from [5] shown in circle markers.

3 Rigid-Wing Simulation Results

The feather angle amplitude of 60° used in the validation case was selected by Nagai *et al.* [5] to correspond with the kinematics observed in actual dragonflies [2]. The effect of this parameter is explored while still maintaining a rigid wing.

Figure 6 shows the lift and power coefficient over the average half-cycle. For the zero-feather case, the wing planform is normal to the flapping-velocity vector, resulting in zero lift force and maximum drag, and therefore the maximum power requirement.

As the feather angle is increased, the power requirement progressively decreases. The net lift increases with θ_0 up to θ_0=50°. For low θ_0 the lift is distributed roughly symmetrically across the half-cycle, while for $\theta_0 \geq 50°$ onwards, the first half of the stroke generates significantly less lift (negative lift for the θ_0=90° case). The maximum instantaneous lift is generated at the θ_0=60° case, but the highest cycle-averaged lift is generated at θ_0=50° (see section 4.1). The power input continues to decrease with θ and the maximum efficiency occurs for θ_0=80°. It is noted for this maximum efficiency case, the time-averaged lift generated is approximately half that obtained in the maximum-lift case (Figure 8b).

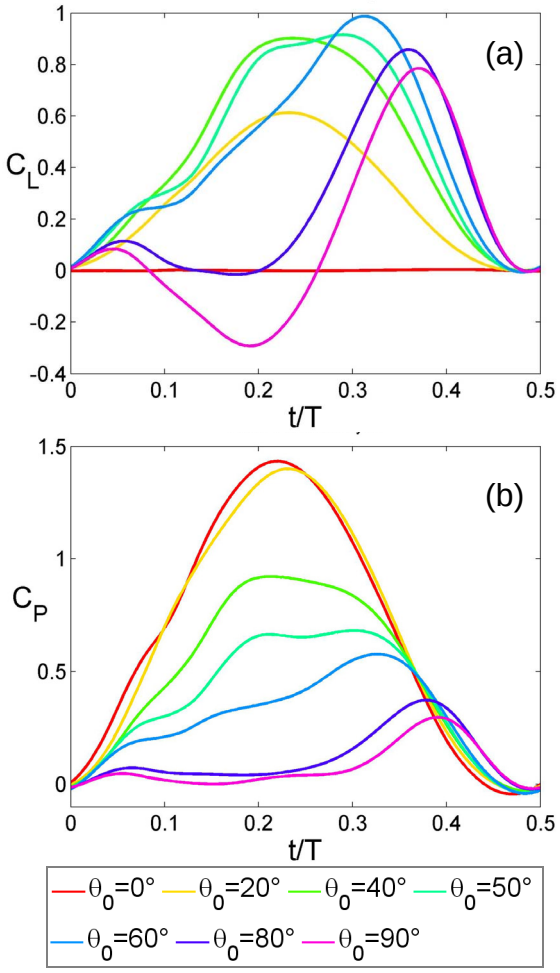

Figure 6 (a) Lift and (b) power, over averaged stroke for rigid-wing cases.

4 Twisting-Wing Simulation Results

4.1 Time-averaged Results

For the twisting results, the flapping amplitude θ_0 is varied linearly from the root value θ_r to the tip value θ_t. A range of θ_r and θ_t values were tested. Therefore for plotting purposes, a single

reference value is used (θ_{ref}), which is the flapping amplitude at the 2/3 span location.

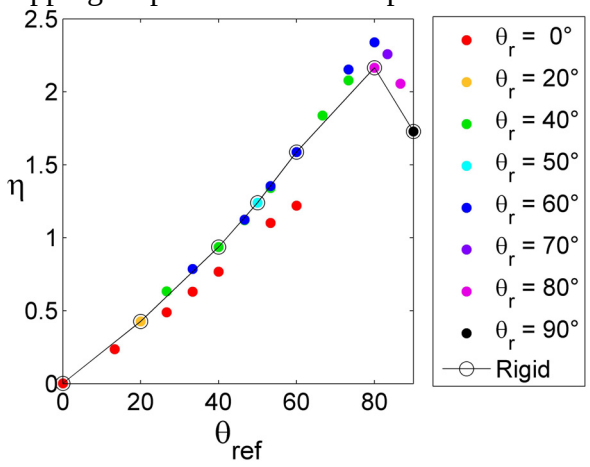

Figure 7 Effect of reference feathering value θ_{ref} on average aerodynamic efficiency.

The cycle-averaged efficiency η is plotted against θ_{ref} in Figure 7 and shows the data to collapse on an approximately linear trend line up to θ_{ref} ~80°, then dropping off. This behavior can be further examined by considering the lift and power separately.

Figure 8(a) shows the cycle-averaged power coefficient against θ_{ref}. The power coefficient decreases monotonically with θ_{ref} and shows an approximately linear trend at intermediate values. With increasing θ_{ref}, the wing chord becomes aligned with the local flow direction and the progressive drop in $\overline{C}_P$ may be attributed to the lower drag force. Increasing θ_{ref} results in a higher feathering motion, and therefore more power consumed in the rotation. However the rotation velocity was calculated to be less than 20% of the flapping velocity, and therefore has a secondary contribution. Figure 8(b) shows the lift against θ_{ref}. For $\theta_r \geq 20°$ the data also collapses on a common trend curve, with a local maximum around θ_{ref} = 40°-50°.

The rigid-wing simulations results discussed in Section 3 are also presented in Figure 7 and Figure 8. It is interesting to note how well this data fits in with the trend of the twisting-wing simulations. These results show that for these kinematics, the performance is primarily determined by the reference feathering amplitude; the degree of spanwise twisting across the wing is secondary.

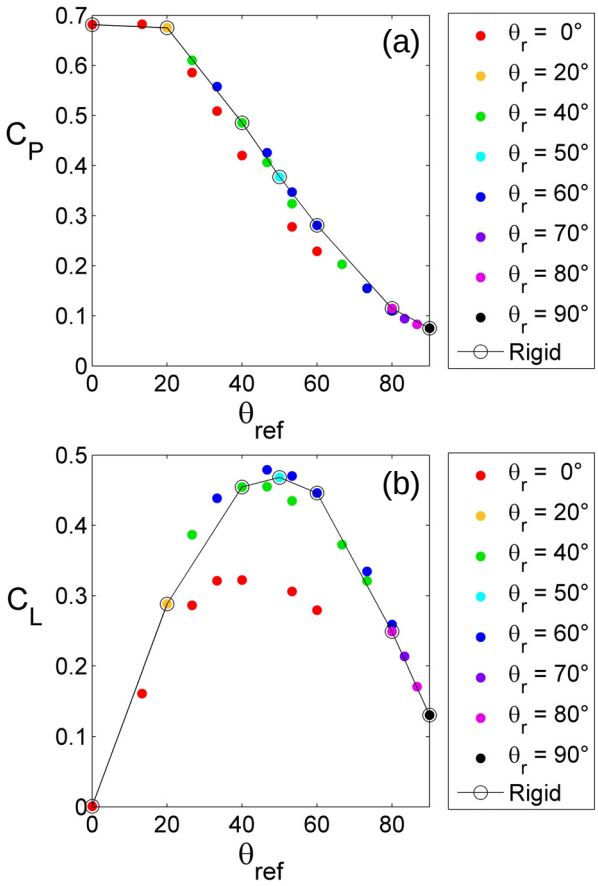

Figure 8 Effect of reference feathering value θ_{ref} on (a) average aerodynamic power requirement and (b) average lift coefficient.

4.2 Zero Root Pitching (θ_r=0°)

As mentioned previously, setting θ_r=0° gives some insight into a passive pitching kinematics. Figure 9 shows the lift generation over an average cycle for the different tip angles. (The corresponding points are also presented in the scatter plots of Figure 7 and Figure 8). With increasing tip feathering angle the peak lift increases up to θ_t~50°, before decreasing and shifting to later in the cycle.

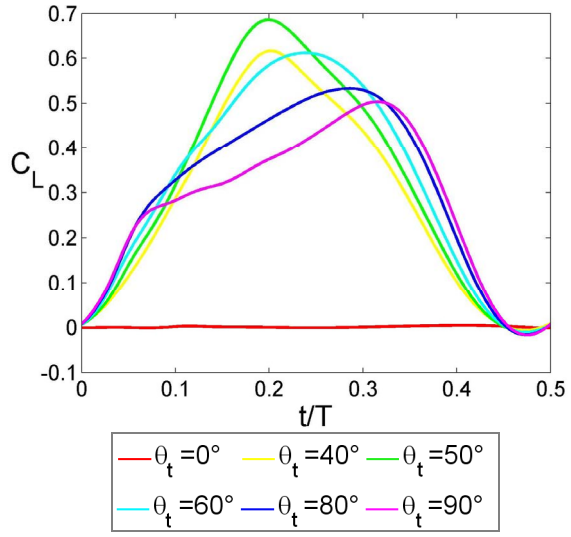

Figure 9 Lift generation over average half stroke for θ_r=0° cases.

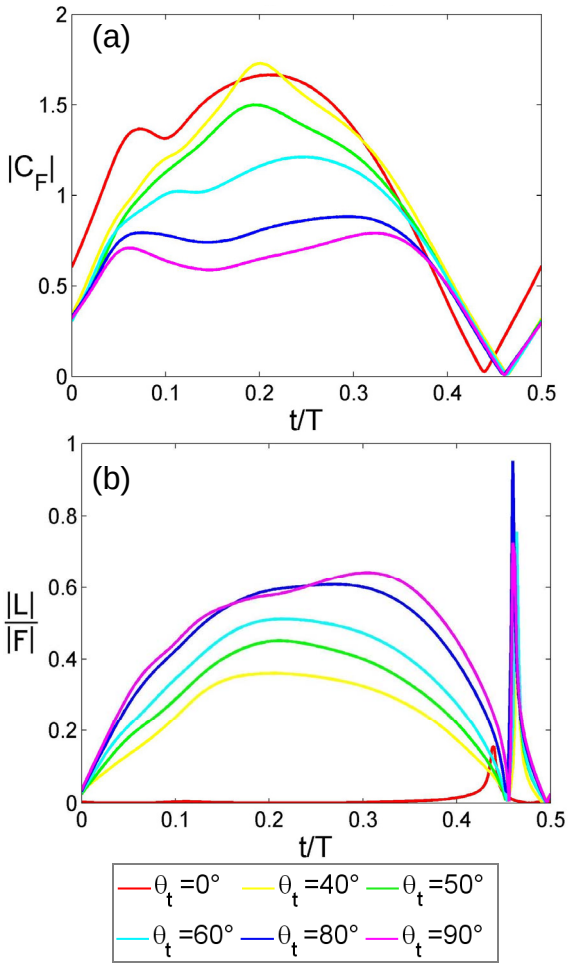

Figure 10 Forces for θ_r=0° cases; (a) magnitude of net force coefficient $|C_F|$ and (b) proportion of total force in the lift direction.

The increase and decrease in the lift generation with θ_t may be explored by considering the effect of θ_t on the net force. The net force is dominated by the pressure component; examination of the data found that pressure contributes at least 85% of the force for most cases across the cycle.

Figure 10(a) shows that as θ_t increases the magnitude of the net force on the wing is decreased. On the other hand, Figure 11(b) indicates that a greater proportion of the force is in the lift direction. With increasing θ_t the wing becomes more aligned with the stroke plane**.** The pressure force acts normal to the wing, which explains why the lift proportion increases with θ_t. The maximum lift condition at θ_t~50° could be considered a compromise between these competing effects.

4.3 Optimal Conditions

From the scatter plots (Figure 7 and Figure 8) it can be seen that the maximum lift condition and maximum efficiency condition occur for θ_r≈60°. These optimal conditions are summarized in Table 1.

Case	θ_r	θ_t	$\overline{C}_L$	$\overline{C}_P$	η
max $\overline{C}_L$	60	40	0.479	0.426	1.12
max η	60	90	0.259	0.111	2.34

Table 1 Twist parameters for optimal lift and efficiency

Peak efficiency is achieved for maximum wingtip feathering. Maximum lift, on the other hand, is achieved for intermediate tip feathering, where the wing remains at a high angle to the flapping-axis at all times. It is noted that this is one of the cases where $\theta_r > \theta_t$.

Figure 11 shows the lift and power generated across an average half-cycle for the two optimal conditions. The maximum lift case shows a larger lift coefficient across the mid-stroke, whereas for the maximum efficiency case, lift is generated mainly over the second half of the stroke. The aerodynamic power requirement for the lift condition is significantly higher however; peak power is more than twice the value for the efficiency condition, and the

power consumption over the cycle is nearly quadrupled.

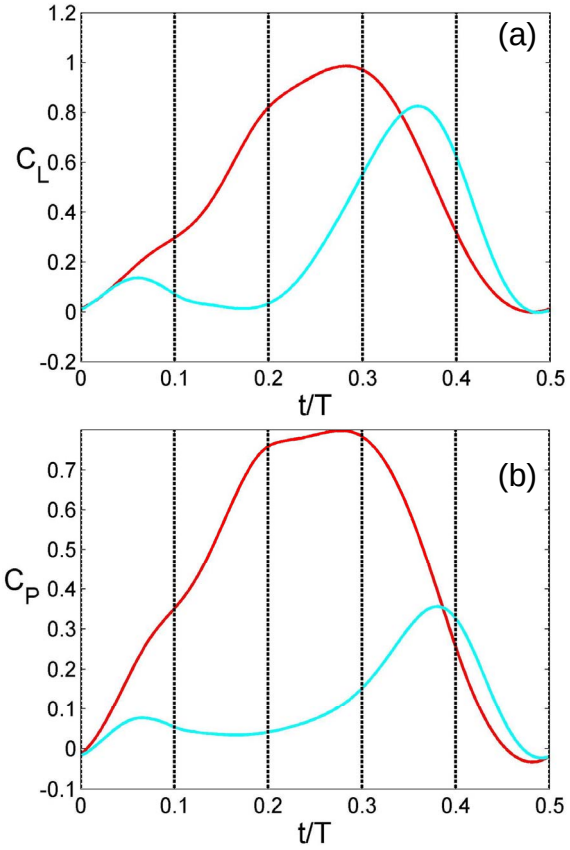

Figure 11 Performance over averaged stroke for optimal conditions: (a) lift coefficient and (b) power coefficient, for optimal lift condition (red) and optimal efficiency condition (blue).

Further insight into the aerodynamic mechanisms of each case can be gained by visualizing the off-body flow structure. Vortex structures can be identified for a velocity field ***v****(x,t)* using the Q-criterion [8], defined as:

$$Q = \frac{1}{2}\left[\left|\Omega\right|^2 - \left|S\right|^2\right] > 0 \qquad (4)$$

where

$$\Omega = \frac{1}{2}\left[\nabla v - (\nabla v)^T\right] \qquad (5)$$

and

$$S = \frac{1}{2}\left[\nabla v + (\nabla v)^T\right] \qquad (6)$$

are the vorticity tensor and rate-of-strain tensor, respectively.

Iso-contours of *Q* plotted at an (arbitrary) level of 50 are presented in Figure 12. The instances in time which are shown correspond to the vertical dashed lines in Figure 11. In both cases, as the wing moves through the stroke, a spanwise structure is generated from the leading edge from the rolling-up of the shear layer. The leading-edge vortex (LEV) has been observed in experiments with insects [9] and mechanical flappers [10], and the high lift necessary to sustain insect flapping flight has been attributed to its presence. The high-lift case is characterized by a larger (LEV), analogous to that observed on a delta wing. This structure intensifies towards the mid-stroke (resulting in a high suction pressure) before degenerating and moving away from the surface towards the end of the stroke.

In contrast, the vortex structures identified in the high-efficiency case are smaller and fairly coherent. The LEV remains attached to the leading edge throughout the stroke, despite the fact that the wing undergoes a greater twist. Additionally a clear tip vortex is observed on the outboard edge of the wing at t/T=0.40.

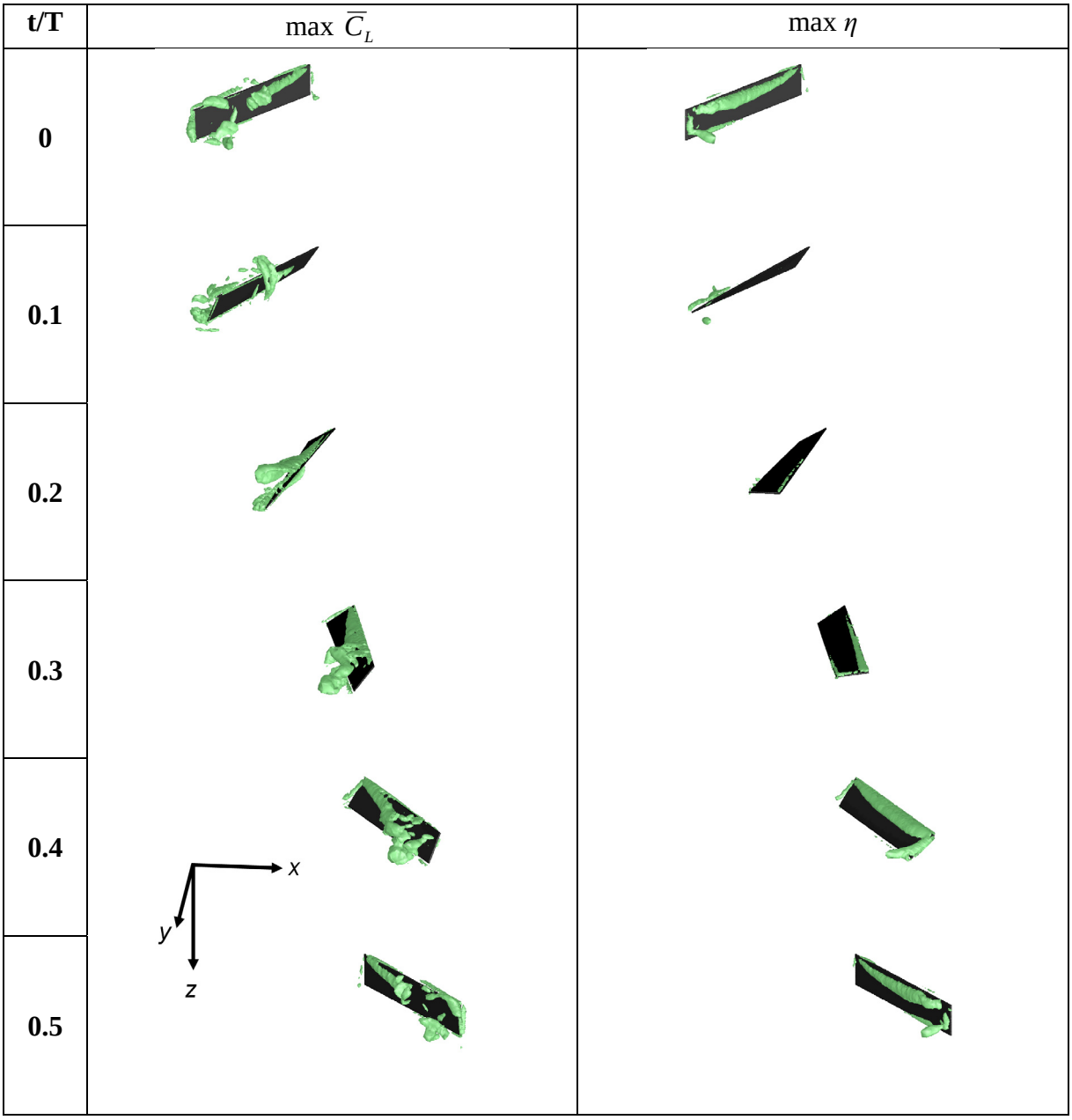

Figure 12 Iso-surfaces of *Q=50* for the maximum $\overline{C}_L$ and η cases.

5 Conclusion

The effect of wing twist angles was investigated for the case of a flapping wing in hover with sinusoidal kinematics. A range of root feathering angles and tip feathering angles were simulated. It was found that in most cases, the power required and the lift generated are dependant mainly on the feathering amplitude at the 2/3 span location. The degree of twist across the wing was not found to be of significance in this study, as most of the results collapsed closely onto a single trend. For the hovering efficiency (defined as the ratio of lift to aerodynamic power required), a linear increase was observed up to a maximum at roughly θ_{ref}=75° (corresponding to the case where θ_r=60°, θ_t=90°). In contrast, the maximum lift was observed around θ_{ref}=40-50°. Examination of the flow structures indicated that the optimal-efficiency case comprised small, coherent,

attached structures, whereas the optimal-lift case exhibited a larger leading edge vortex which degenerated during the cycle. This suggests that there are two different flow regimes for this type of flapping kinematics. From a MAV perspective, the flexibility (and therefore structural) wing requirements will depend on which regime is most desirable.

6 References

[1] Ellington C. P. The novel aerodynamics of insect flight: applications to micro-air vehicles. *J. Exp. Biology*, Vol. 202, pp. 3439-3448, 1999.

[2] Azuma A. and Watanabe T. Flight Performance of a Dragonfly. *J. Exp. Biology*, Vol. 137, pp. 221-252, 1988.

[3] Hamamoto M., Ohta Y. and Hara K. Design of Flexible Wing for Flapping Flight by Fluid-Structure Interaction Analysis. *Proceedings IEEE Int. Conf. Robotics and Automation* pp. 2253-2258, 2005.

[4] Heathcote S., Wang Z. and Gursul I. Effect of spanwise flexibility on flapping wing propulsion. *J. Fluids and Structures*, Vol. 24, pp.183-199, 2008.

[5] Nagai H., Isogai K. and Fujimoto T. Experimental Study on Flow Interaction Between Fore- and Hindwings of Dragonfly in Hovering and Forward Flight. *Proceedings 27th Council of the Aeronautical Sciences*, Paper No. ICAS2010-3.1.2, 2010.

[6] Nagai H., Personal communication, 2011.

[7] ANSYS, Inc., Canonsburg, Pennsylvania, USA, http://www.ansys.com/Products/Simulation+Technology/Fluid+Dynamics/ANSYS+Fluent, accessed 13 March 2012

[8] Hunt J. C. R., Wray A. and Moin P. Eddies, stream, and convergence zones in turbulent flows. *Center for Turbulence Research Report* CTR-S8, 1988, cited in Haller G. An objective definition of a vortex. *Journal of Fluid Mechanics*, Vol. 525, pp 1-26, 2005.

[9] Ellington, C.P., Van Den Berg, C., Willmott, A. P. and Thomas, A. L. R. Leading-edge vortices in insect flight. Nature, Vol. 384, pp 626-630, 2006.

[10] Birch, J.M. and Dickinson, H. H. Spanwise flow and the attachment of the leading-edge vortex on insect flight, Nature, Vol. 412, pp 729-33, 2001.

[11] Lu, Y. Shen, G. X. and Lai, G. J. Dual leading-edge vortices on flapping wings, J. Exp. Biology, Vol. 209, pp. 5005-5016, 2006.

Copyright Statement